

# Statistical Characterization of 300 GHz Propagation on a Desktop

Seunghwan Kim *Student Member, IEEE*, and Alenka Zajić *Senior Member, IEEE*

**Abstract**—This paper presents measurements and statistical characterization of 300 – 320 GHz desktop channels. The measurements are performed in line-of-sight (LoS) and non-line-of-sight (NLoS) environments. From the large set of LoS measured data, the parameters for single-slope path loss model with shadowing are devised. The results show that the path loss exponent is around 1.9 and the variations due to shadowing are similar across different frequencies and different bandwidths. Furthermore, the impact of different materials on the path loss is studied in NLoS environment. The results show that metal objects in the propagation path cause multiple strong reflections leading to higher path loss. Furthermore, the statistical analysis of multipath propagation is performed. The rms delay spread, the mean excess delay, the maximum excess delay, and the coherence bandwidth for LoS and NLoS environments are calculated. The results show that the mean excess delay and rms delay spread increase with distance and that the rms delay spread in desktop THz channel is much smaller than in typical indoor ultra-wideband channels. In addition, the power delay profiles for LoS and NLoS environments are analyzed. The results show that strong reflections from the transmitter and receiver electronics are present both in LoS and NLoS environments. Finally, the statistical analysis of the measured signal amplitude in LoS and NLoS environments is performed. For both LoS and NLoS propagation environment, it is found that lognormal distribution provides the best fit.

**Index Terms**—THz channels, indoor channels, statistical characterization, channel sounding.

## I. INTRODUCTION

Ultra-broadband Terahertz (THz) communication systems are expected to help satisfy the ever-growing need for smaller devices that can offer higher speed wireless communication anywhere and anytime. In the past years, it has become obvious that wireless data rates exceeding 10 Gbit/s will be required in several years from now [1]. The opening up of carrier frequencies in the terahertz-range is the most promising approach to provide sufficient bandwidth required for ultra-fast and ultra-broadband data transmissions [2]. A suitable frequency window can be found around 300 GHz, offering an unregulated bandwidth of 47 GHz [2]. This large bandwidth paired with higher speed wireless links can open the door to a large number of novel applications such as ultra-high-speed pico-cell cellular links, wireless short-range communications, secure wireless communication for military and defense applications, and on-body communication for health monitoring systems.

Paper approved by Dr. Claude Oestges, the Associate Editor for IEEE Transactions on Vehicular Technology. Manuscript received December 09, 2013; revised June 03 2014, July 18, 2014, and September 01 2014.

Seunghwan Kim and Alenka Zajić are with the School of Electrical and Computer Engineering, Georgia Inst. of Tech., Atlanta, GA 30332 USA

There are two main approaches to generating terahertz radiation [2]. The first approach translates optical frequencies into the terahertz range, i.e. continuous or pulsed terahertz radiation is generated by laser excitation of semiconductors, or lasers and nonlinear crystals are directly operated at terahertz frequencies. The second approach uses frequency multipliers to increase operating frequencies of electronic devices from the millimeter-wave to terahertz range.

Using the first (optical→terahertz) approach, there are a few potential methods for generating THz continuous-wave radiation and they are based on either infrared-pumped gas lasers or on photo-mixing [3]-[5]. Recently, researchers at NTT and Osaka University have demonstrated a possibility of THz communication in the 250 GHz and 300 GHz frequency bands [6], [7] using the photonic technology.

Using the second (mm-wave→terahertz) approach, there are several techniques that offer encouraging prospects for all-electronic solutions for wireless communication systems at terahertz frequencies [8], [9]. One of them is Schottky-diode-based multiplying to increase operating frequencies of electronic devices from the millimeter-wave to terahertz range, which is used in our measurement setup described in Section II. Using all electronic components for both the transmitter and receiver, Jastrow *et al.* [10], [11] have demonstrated the transmission of analog and digital video signals in the 300 GHz band using 10 GHz of available bandwidth.

Overall, both the optical→terahertz and the mm-wave→terahertz approaches offer several promising paths for future integration of terahertz transceivers into future communication systems. Regardless of which technology becomes prevalent, to enable future terahertz-range wireless communications, it is imperative to understand propagation mechanisms that govern communication at 300 GHz and to develop statistical models that can be used to describe general channel properties needed for system design or for algorithm testing.

The first free-space measurements at 300 GHz with bandwidth of 10 GHz have been reported in [12]-[14] for two indoor scenarios: 1) a free-space link of devices on a desktop and 2) a free-space connection of a laptop to an access point in the middle of an office. Additionally, ray-tracing models have been reported in [15]-[19]. However, no statistical characterization of 300 GHz channel has been reported so far. To address this problem, we have performed line-of-sight (LoS) and non-line-of-sight (NLoS) measurements at 300 GHz with larger available bandwidth (i.e. 20 GHz of bandwidth) between the transmitter  $T_x$  and the receiver  $R_x$  on a desktop. The contributions of this paper are:

- 1) Devised parameters for the single-slope path loss model with shadowing for LoS environment and analyzed the impact of different materials on path loss when there is no direct line-of-sight present. The results show that the path loss exponent is around 1.9 and the variations due to shadowing are similar across different frequencies and different bandwidths. Additionally, we find that metal objects in the propagation path cause multiple strong reflections leading to higher path loss.
- 2) Analyzed the rms delay spread  $\tau_{rms}$ , the mean excess delay  $\tau_m$ , the maximum excess delay, the coherence bandwidth and power delay profiles for LoS and NLoS environments. In LoS environment, the mean values of  $\tau_{rms}$  and  $\tau_m$  are 428.4 ps and 90.21 ps, respectively, and the variances are 238 ps and 24.56 ps, respectively. The results show that the mean excess delay and rms delay spread increase with distance and that the rms delay spread in desktop THz channel is much smaller than in typical indoor ultra-wideband channels. From power delay profiles, we have observed that the strong reflections from the transmitter and receiver electronics are present both in LoS and NLoS environments.
- 3) Performed statistical analysis of the measured signal amplitude in LoS and NLoS environments. For both LoS and NLoS propagation environment, it is found that lognormal distribution provides the best fit.
- 4) Analyzed the temporal correlation functions for LoS and NLoS environments. The results show that correlation function drops below 0.2 after 0.15 ns. However, if the strong reflected paths are present in the channel, correlation function can increase above 0.2 and the signals may get correlated again. This corresponds to the findings in power delay profile where strong reflected paths are present in the channel much after the first path has arrived due to reflections from the transmitter and receiver electronics.

The remainder of the paper is organized as follows. Section II describes the measurement equipment, antennas used in the measurements, and the measurement sites. Section III presents the path loss, shadowing, and multipath propagation analysis of measured data. Finally, Section IV provides some concluding remarks.

## II. MEASUREMENT SETUP

### A. Equipment

The measurement setup consists of the N5224A PNA vector network analyzer (VNA), the VDI transmitter (Tx210) and the VDI receiver (Rx148). The N5224A PNA VNA provides input signal in the range 10 MHz–20 GHz. In the VDI Tx210 transmitter, the terahertz-range carrier signal starts out as a 25 GHz signal, which is generated by a Herley-CTI phase-locked dielectric resonator oscillator (DPRO with 100 MHz reference crystal oscillator) [20]. This signal is amplified and its frequency is doubled using Norden N08-1975 [21], and then its frequency is tripled using VDI WR6.5X3 [22]. This signal is then fed to a sub-harmonic mixer (WR2.8SHM) that plays a dual role of doubling the carrier frequency and mixing it with

the baseband signal (10 MHz–20 GHz, delivered by the VNA) [23]. The terahertz-range signal is then transmitted by the horn antenna that has a gain of 26 dBi in the range 280–320 GHz. At the receiver side, the same components are used to down-convert the signal, except that the DPRO is tuned to 24.2 GHz. This results in a down-conversion of the received signal to an intermediate frequency (IF) of 9.6 GHz. The upper sideband of the down-converted signal is then recorded by the VNA in the frequency range of 9.6–29.6 GHz. The corresponding block diagram is shown in Fig. 1.

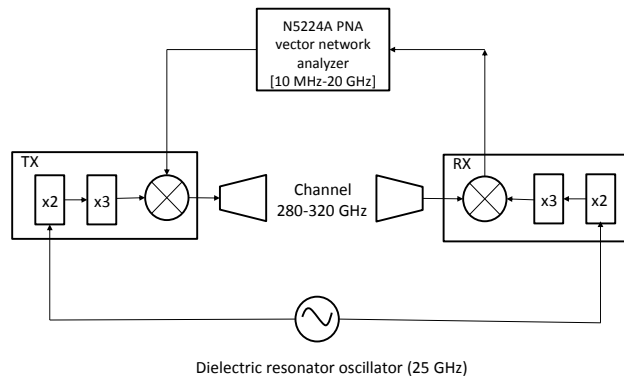


Fig. 1. The 280–320 GHz channel measurement setup.

By recording the frequency dependent scattering parameter  $S_{21}$  for the test signal frequencies  $f_{\text{test}} = 10 \text{ MHz} - 20 \text{ GHz}$  at the VNA, the channel transfer function at  $f = 300 \text{ GHz} + f_{\text{test}}$  is measured. The maximum allowable input power is 0 dBm (1 mW) which allows for communication at the maximum distances of about 1 m without additional optical lenses. Although propagation loss at terahertz frequencies is significant, high antenna gains would be sufficient to compensate for most of that loss and allow for longer distances. However, the loss in the transceiver is very high and antenna gain barely compensates for the losses in the system. To illustrate the transceiver losses, Fig. 2 shows the transfer function  $S_{21}$  of the system when the transmitter ( $T_x$ ) and the receiver ( $R_x$ ) are directly connected (without antennas). Since the system calibration could only be performed at the input and the output of the mixers, additional deembedding is performed by correcting the amplitude of the measured transfer function for the losses in transceiver.

The full available bandwidth of 19.99 GHz is used in all measurements which provides the spatial and temporal resolution of 1.5 cm or 0.05 ns. The start frequency is bound to a minimum of 10 MHz by the VNA and the stop frequency could not exceed the system limitations of 20 GHz. Due to input power restrictions of the mixers, a test signal with a power of  $-10 \text{ dBm}$  is used, providing a dynamic range of approximately 90 dB for the chosen intermediate frequency filter bandwidth of  $\Delta_{IF} = 20 \text{ kHz}$ . The number of sweep points is set to 801, and the maximum excess delay is 40 ns. All measurement parameters are summarized in Table I.

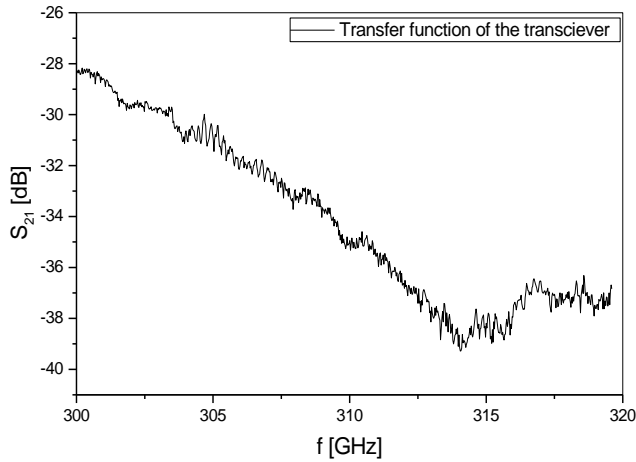


Fig. 2. Amplitude response of the 300 GHz measurement system (without antennas).

TABLE I  
MEASUREMENT PARAMETERS.

Parameter	Symbol	Value
Measurement points	$N$	801
Intermediate frequency bandwidth	$\Delta f_{IF}$	20 kHz
Average noise floor	$P_N$	-100 dBm
Input signal power	$P_{in}$	-10 dBm
Start frequency	$f_{start}$	10 MHz
Stop frequency	$f_{stop}$	20 GHz
Bandwidth	$B$	19.99 GHz
Time domain resolution	$\Delta t$	0.05 ns
Maximum excess delay	$\tau_m$	40 ns

### B. Antenna Characteristics and Site Description

For this measurement campaign, two horn antennas with 26 dBi gain are used. Both antennas are vertically polarized and mounted about 1.5 cm above the ground. The theoretical half power beam-widths (HPBW) are about  $10^\circ$  in azimuth and elevation. The measured return loss of the horn antenna used in the measurements is shown in Fig. 3. We can observe that the antenna has  $S_{11}$  lower than  $-10$  dB in the range 300–320 GHz. In the further analysis, the antennas are considered to be part of the transfer function.

Typical line-of-sight (LoS) communication between devices on a desktop can be expected to operate at distances between 5 cm and 70 cm. Hence, in the first measurement scenario, we have collected channel transfer functions in this range of distances using the measurement setup shown in Fig. 4 (a) at the locations shown in Fig. 4 (b). The module spacing has been varied by moving the  $R_x$  and keeping the  $T_x$  fixed.

The second measurement scenario tests non-line-of-sight (NLoS) type of communication shown in Fig. 4 (c). The  $T_x$  and the  $R_x$  are positioned orthogonal to each other (i.e., the  $T_x$  antenna is parallel with  $y$ -axis and the  $R_x$  antenna is

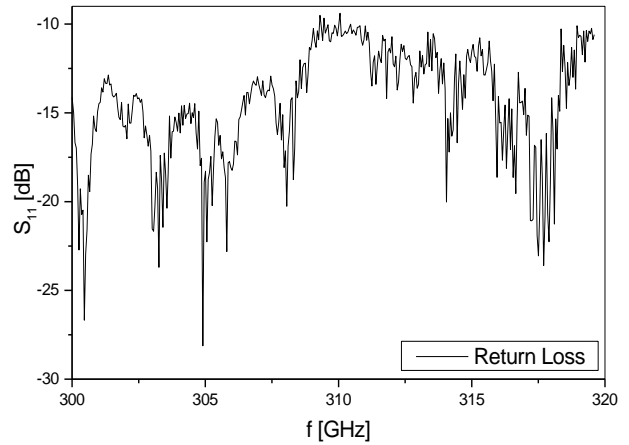


Fig. 3. Measured  $S_{11}$  of the horn antenna as a function of frequency.

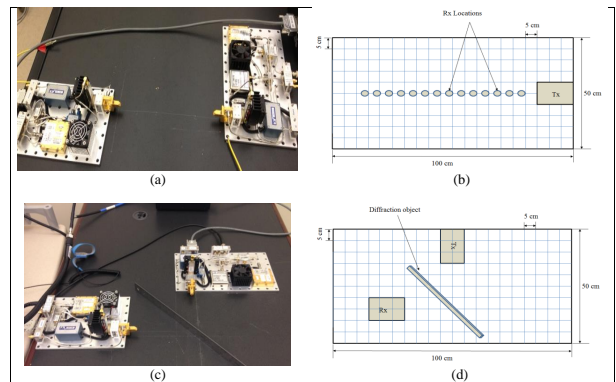


Fig. 4. (a) Measurement setup for LoS channel characterization; (b) Measurement setup for NLoS channel characterization.

parallel with  $x$ -axis) with the equal distances from the  $T_x$  antenna to center of the table and from the center of the table to the  $R_x$  antenna. These distances were 21.25 cm, i.e., the diagonal distance between the  $T_x$  and  $R_x$  antennas was  $d = 30$  cm. Three types of material, FR4, metal, and plastic are placed at  $45^\circ$  degree between the  $T_x$  and the  $R_x$ , as shown in Fig. 4 (d). Note that the different materials used as obstacles have 10 cm height and were completely blocking the line-of-sight between the  $T_x$  and  $R_x$  antennas, so the only possible way for communication is via diffraction or reflection.

The transfer function is recorded before different materials are placed between the  $T_x$  and the  $R_x$  and the  $S_{21}$  was near noise level indicating that there is not communication between the  $T_x$  and the  $R_x$ . By using different objects to diffract the signal, communication was successfully established and the next section discusses the obtained results.

### III. STATISTICAL CHARACTERIZATION OF THE 300 GHz CHANNEL

Site-specific prediction requires detailed knowledge of the propagation environments. When such information is not available, statistical models can be used to describe general channel properties which are useful for system design or for algorithm testing. Note that statistical characteristics of the measured

channel will be dependent on antennas and their locations. This section presents the key statistical parameters extracted from all collected measurements.

### A. Path Loss and Shadowing

In this paper, we refer to mean path loss as the transmit power multiplied by the transmit and receive antenna gains divided by the mean received power, i.e.,

$$PL = \frac{P_t \cdot G_t \cdot G_r}{\bar{P}_r} \quad (1)$$

The local mean path loss is obtained by averaging a swept continuous wave over time and frequency, i.e.,

$$PL(d) = \frac{1}{MN} \sum_{i=1}^N \sum_{j=1}^M |H(f_i, t_j, d)|^2, \quad (2)$$

where  $H(f_i, t_j, d)$  is the measured complex frequency response data matrix,  $N$  is the number of observed frequencies,  $M$  is the number of frequency-response snapshots over time, and  $d$  is the distance in meters.

In the first measurement scenario, LoS communication between devices on a desktop is tested in a measurement setup shown in Fig. 4 (a). In these experiments, the number of observed frequencies was  $N = 801$ , the number of frequency-response snapshots over time was  $M = 10$  (scatter plot in Fig. 7 shows that this is sufficient), and the distances were varied from 5 cm to 70 cm with step of 5 cm.

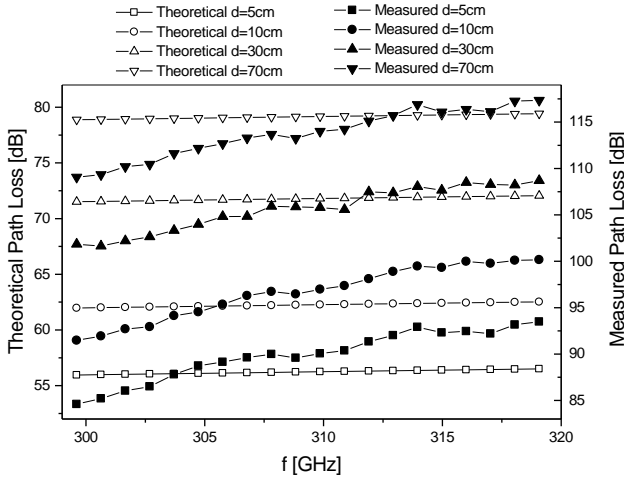


Fig. 5. Measured and theoretical path loss as a function of frequency in LoS environment.

Figure 5 shows the measured path loss as a function of frequencies for several distances between the  $T_x$  and the  $R_x$ , when the losses in the transceiver are not removed from the measured transfer function. We can observe that the path loss significantly increases with frequency and does not follow the path loss predicted by the Friis equation in (1). The reason for this discrepancy is the frequency dependent transfer function of the transceiver shown in Figure 2. When the additional deembedding is performed, by correcting the amplitude of the measured transfer function for the losses in

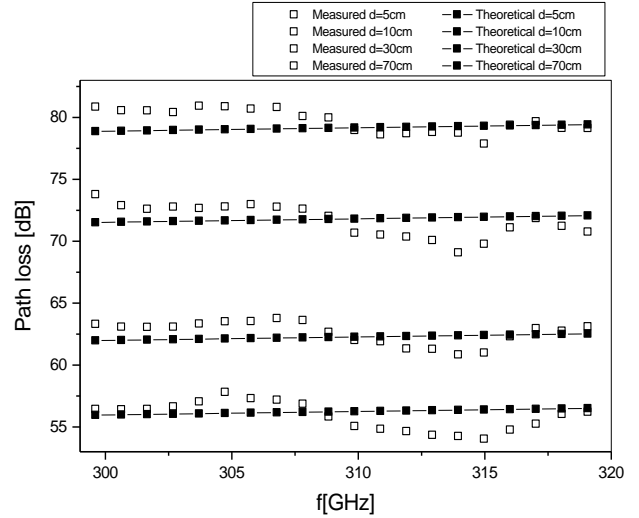


Fig. 6. Deembedded measured and theoretical path loss as a function of frequency in LoS environment.

the transceiver, better match is observed between the measured and theoretical path loss, as shown in Fig 6. However, the path loss variation observed across the frequencies indicates that channel equalization across such a wide frequency range is not a straight forward task. In the remaining of the paper, we will use deembedded results to capture true nature of the propagation environment.

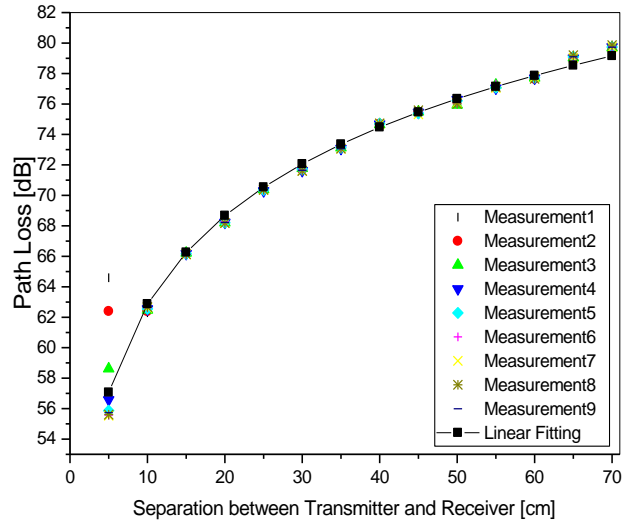


Fig. 7. Scatter plot of the path loss versus T-R separation in LoS environment.

Figure 7 shows the scatter plot of the path loss as a function of transmitter-receiver (T-R) separation on a desktop for a LoS environment. We can observe that except for 5 cm distance, the variation between different frequency-response snapshots over time is minimal. This is because there are no temporal or spatial variations nor additional clutter in the channel that would cause significant variations in the measured path loss. The variations in path loss at 5 cm or shorter distances are

due to difficulty to achieve very precise alignment between two antennas. Note that this finding is significantly different from typical indoor measurements, where path loss significantly varies around the mean value. This finding leads us to conclude that the number of frequency-response snapshots over time does not have to be large and we have found that 10 measurements are sufficient to capture all temporal variations in the signal. However, we still observe some shadowing in our measurements. This is caused by small variations in alignment between the Tx and Rx antenna. While this may not be a traditional shadowing process, it is a random process that causes variations of the received power at a given distance, as shown in Fig. 8.

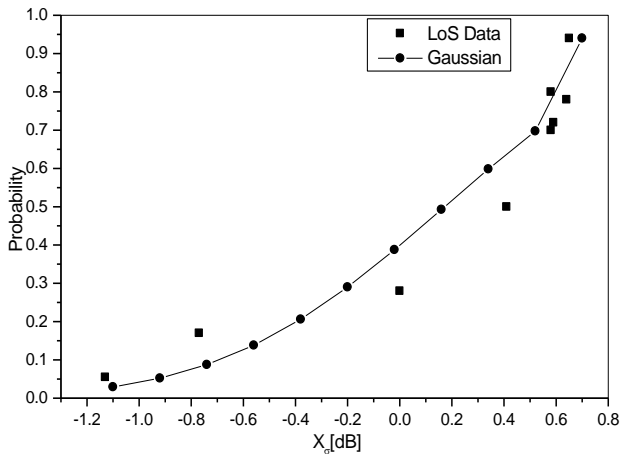


Fig. 8. Confirming the log-normality of shadow fading in LoS environment.

Path loss over distance can be modelled by the path-loss exponent model as follows [24]

$$PL(d) = 10\gamma \log_{10} \left( \frac{d}{d_0} \right) + PL(d_0) + X_\sigma, \quad (3)$$

where  $PL(d)$  is the average path loss in dB at the distance  $d$ ,  $PL(d_0)$  is the free-space path loss at the reference distance  $d_0$ ,  $\gamma$  is the path loss exponent that characterizes how fast the path loss increases with the increase of the separation between the  $T_x$  and the  $R_x$ , and  $X_\sigma$  represents shadow fading that can be modeled as a zero-mean Gaussian distributed random variable (in dB) with standard deviation  $\sigma$ .

To estimate the path-loss model parameters  $\gamma$  and  $\sigma$ (dB) in (3), we have performed the least-squares linear regression fitting through the scatter of measured path loss points in decibels such that the root-mean square deviation of path loss points about the regression line is minimized. The model parameters and standard deviations are estimated for the 20 GHz frequency bandwidth, as well as for 2.5 GHz bandwidth starting at  $f = \{300, 305, 310, 315\}$  GHz, respectively. The reference distance is  $d_0 = 1$  m and the free-space path loss at the reference distance  $d_0$  is  $PL(d_0) = 81.97$  dB. The results are summarized in the Table II and the fitting of the path loss scatter plot is shown in Fig. 6. The results show that the path loss exponent is around 1.9 and the variations due to shadowing are similar across different frequencies

and different bandwidths. To confirm that shadowing can be modeled as a zero-mean Gaussian distributed random variable, we have compared the measured distribution of shadow fading with the Gaussian distribution in Fig. 8.

TABLE II  
PATH LOSS PARAMETERS.

Frequency [GHz]	LoS Propagation			
	Path loss exponent $\gamma$	Standard deviation	Variance $\sigma$ [dB]	Standard deviation
300-320	1.927	0.058	0.67	0.173
300-302.5	1.916	0.045	0.67	0.17
305-307.5	1.886	0.06	0.715	0.185
310-312.5	1.93	0.061	0.737	0.19
315-317.5	1.95	0.056	0.71	0.18

The second measurement scenario assumes NLoS type of propagation. The number of observed frequencies was  $N = 801$  and the number of frequency-response snapshots over time was  $M = 10$ . The  $T_x$  and the  $R_x$  are positioned orthogonal to each other with the diagonal distance between them set to  $d = 30$  cm. FR4, metal, and plastic are placed at  $45^\circ$  degree between the  $T_x$  and the  $R_x$ , as shown in Fig. 4 (b). Figure 9 compares the measured path loss as a function of frequencies for signals diffracted of FR4, metal, and plastic material with the theoretical free-space path loss. We can observe that the path loss of signals reflected from FR4 and plastic are oscillating around the theoretical free-space path loss. However, signals reflected from metal have additional 5 dB of loss. We have found that metal objects in the propagation path cause multiple strong reflections which is probably leading to higher path loss.

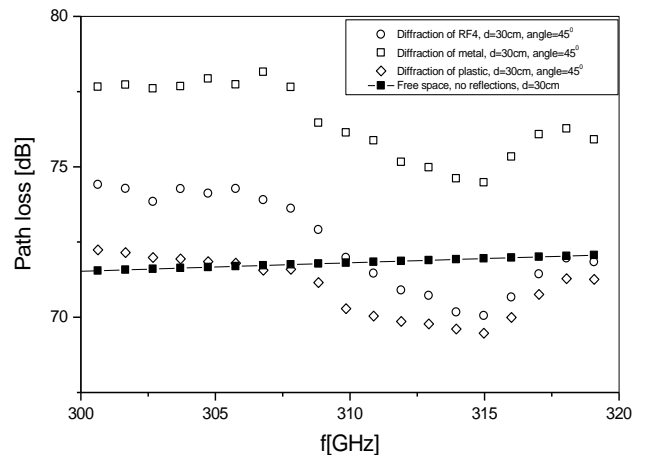


Fig. 9. Measured diffracted path loss and theoretical free-space path loss as a function of frequency.

### B. Multipath Characterization

Multipath propagation is the propagation mechanism manifested when the transmitted signal reaches the receive antenna along two or more paths. Such waves typically arrive at the receiver from many different directions and with different delays, and combine vectorially at the receiver antenna. Such

channel impulse response can be characterized as [25]

$$h(t, \tau, d) = \sum_{k=1}^L a_k(t, d) \exp(j\theta_k(t, d))\delta(t - \tau_k), \quad (4)$$

where,  $N$  is the number of multipath components,  $a_k$  represents the amplitude of the  $k^{th}$  multipath component,  $\theta_k$  is the associated phase, and  $\tau_k$  is the excess delay of the  $k^{th}$  path relative to the first arrival, and  $\delta(\cdot)$  denotes the Dirac delta function.

An estimate of the channel impulse response is made by taking the inverse discrete Fourier transform (IDFT) of the measured frequency response. The impulse response is then normalized such that the area under the squared magnitude of the power-delay response is equal to one. We refer to a normalized squared magnitude of the impulse response as the multipath intensity profile (MIP) at the single point in space. The noise floor of the MIP is set to 10 dB above the average receiver noise floor. Part of the MIP characterization is based on root mean square (rms) delay spread  $\tau_{rms}$ , which is a measure of multipath spread within the channel. It is an important parameter for characterizing time dispersion or frequency selectivity. It is the square root of the second central moment of the MIP and is given by [25]

$$\tau_{rms} = \sqrt{\sum_{k=1}^L (\tau_k - \tau_m)^2 |h(t, \tau_k, d)|^2}, \quad (5)$$

where  $\tau_m$  is the mean excess delay (the first moment of the MIP) and is defined as

$$\tau_m = \sum_{k=1}^L \tau_k \cdot |h(t, \tau_k, d)|^2. \quad (6)$$

For LoS environment, Fig. 10 shows that the rms delay spread is normally distributed over all distances. The threshold level in decibels was chosen to be  $-30$  dB from the maximum received power because approximately 99% of the power is captured with this threshold. The mean values of  $\tau_{rms}$  and  $\tau_m$  are 428.4 ps and 90.21 ps, respectively, and the variances are 238 ps and 24.56 ps, respectively. Figure 11 shows the path loss versus rms delay spread. The mean  $\tau_{rms}$  and the mean path loss were obtained by averaging over 10 measured channel impulse responses. Note that similar results are obtained when averaging over 500 measured channel impulse responses. The results indicate an increase in  $\tau_{rms}$  with increasing path loss. This is an anticipated result, since the paths with longer delays have also larger path loss values associated with them. Finally, the rms delay spread, the mean excess delay, the maximum excess delay, and the coherence bandwidth ( $B_c = 1/(2 \cdot \pi \cdot \tau_{rms})$ ) are compared for different distances. A summary of these results is given in Table III. The results show that the mean excess delay and rms delay spread increase with distance as expected. Furthermore, the results show that the rms delay spread in desktop THz channel is much smaller than in typical indoor ultra-wideband channels. Finally, the results show that the coherence bandwidth significantly reduces with distance. For distances of 5 cm or shorter, the whole 20 GHz bandwidth can be used as a narrowband channel. However, for

longer distances, the coherence bandwidth reduces to couple hundred of megahertz.

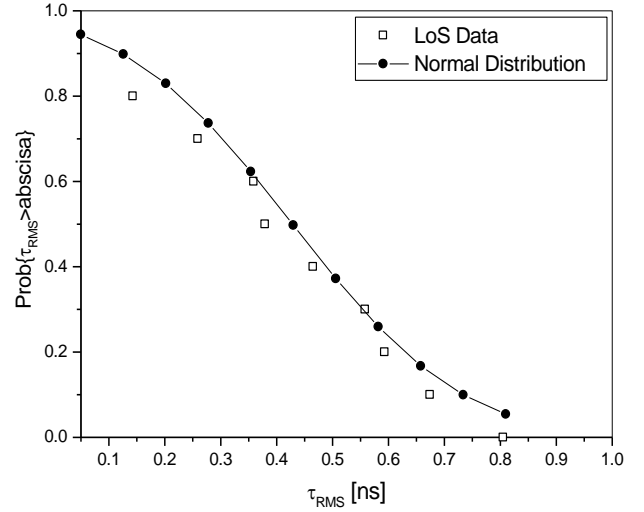


Fig. 10. Cumulative distribution function of rms delay spread in LoS environment.

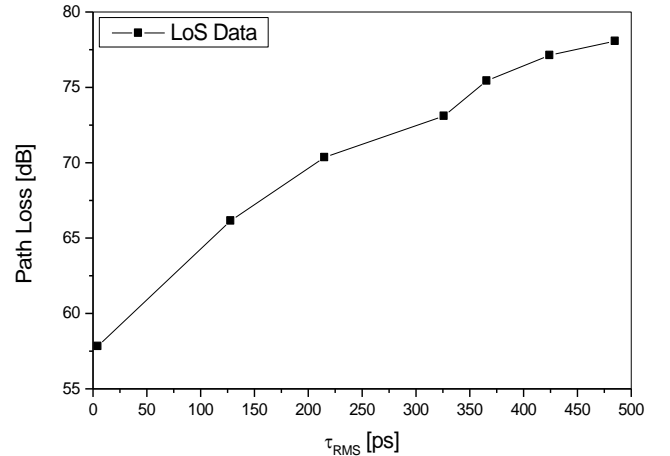


Fig. 11. Path loss versus rms delay spread in LoS environment.

For NLoS environment, the rms delay spread, the mean excess delay, the maximum excess delay, and the coherence bandwidth are compared for different materials. A summary of these results is given in Table IV. Here, the threshold level in decibels was chosen to be  $-35$  dB from the maximum received power. For plastic and FR4, 98.5% of the power was captured with this threshold, while for metal, 96.9% of the power was captured with this threshold. The results show that diffraction of metal has slightly higher coherence bandwidth than diffraction of FR4 and plastic. Furthermore, we can observe that the mean excess delay, the maximum excess delay, and the coherence bandwidth for these three materials is comparable with those of LoS propagation with the T-R spacing of 25 cm-30 cm.

Here, we also calculate the power delay profile (PDP) by averaging the magnitude squared of the channel impulse

TABLE III

MEAN EXCESS DELAY, RMS DELAY SPREAD, MAXIMUM EXCESS DELAY, AND COHERENCE BANDWIDTH FOR DIFFERENT T-R SPACINGS.

Distance [cm]	$\tau_m$ [ps]	$\tau_{rms}$ [ps]	$\tau_{max}$ [ns]	$B_c$ [GHz]
5	50.76	4.35	0.1	36.6
15	63.73	127.79	1.45	1.24
25	74.61	215.05	2.15	0.74
35	100.44	326.01	2.75	0.488
45	123.05	365.69	3.9	0.435
55	158.39	424.15	4.2	0.375
65	176.46	484.94	4.65	0.328

TABLE IV

MEAN EXCESS DELAY, AND RMS DELAY SPREAD FOR DIFFERENT DIFFRACTION MATERIALS.

Material	$\tau_m$ [ps]	$\tau_{rms}$ [ps]	$\tau_{max}$ [ns]	$B_c$ [GHz]
FR4	70.53	210	2.65	0.757
Metal	67.07	187	2.5	0.85
Plastic	77.54	227	3.05	0.701

response over the number of frequency-response snapshots

$$P(\tau) = \frac{1}{M} \sum_{k=1}^M |h(t_k, \tau, d)|^2, \quad (7)$$

where  $t_k$  is the fixed observation instant of the  $k^{th}$  frequency-response snapshots and  $M$  is the total number of frequency-response snapshots.

For LoS propagation environment, power delay profiles for distances  $d = \{10, 15, 20, 40, 70\}$  cm between the  $T_x$  and the  $R_x$  are shown in Fig 12. The significant part of the PDP is determined by discarding all parts that are more than 35 dB down from the strongest path, because approximately 99.5% of the power is captured with this threshold. The results show that in addition to the direct path, there is an additional strong reflection component. From the time of arrival, we can conclude that this reflection is from the signal that was once reflected from the  $R_x$  electronics, then reflected from the  $T_x$  electronics and then received at the  $R_x$ . This conclusion is also verified experimentally by putting absorbers around the  $T_x$  and  $R_x$  antennas, blocking the paths toward the electronics. We have observed that the strong reflections would disappear from the power delay profile. This is an interesting observation that opens up the question of putting the absorbers around the antennas. We choose not to use the absorbers, because in practice, even if we manage to perfectly shield the  $T_x$  and  $R_x$  electronics, there might be objects in the vicinity or behind the  $T_x$  or  $R_x$  that can create similar propagation effects. This result also explains somewhat large rms delay spreads in Table III.

For NLoS propagation environment, Figure 13 compares the normalized power delay profile of signals diffracted from FR4, metal, and plastic. The diagonal separation between the  $T_x$  and  $R_x$  antennas was 30 cm. The results show that

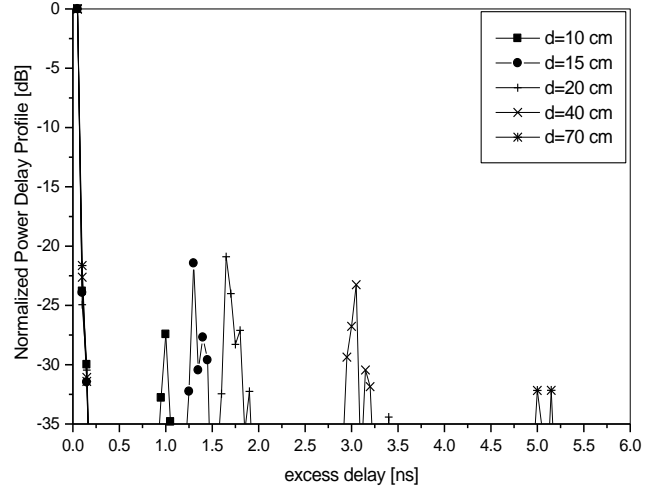


Fig. 12. Normalized power delay profile in LoS propagation environment.

there is a diffracted path, and somewhat surprisingly, there are several strong reflected paths. By examining the time of arrival, we have found that these reflections are multiple reflections from the  $R_x$  and  $T_x$  electronics. Furthermore, we can observe that diffractions and reflections from metal have stronger multipath components and keep arriving with power higher than  $-40$  dB for more than 7ns. This indicates that if rich multipath is present in the channel, there will be large number of paths arriving with significant amount of energy which would require sophisticated channel equalization schemes.

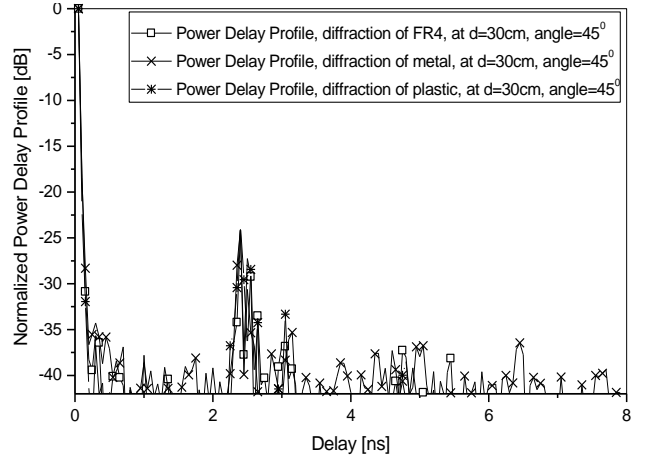


Fig. 13. Normalized power delay profile in NLoS propagation environment.

To test the statistical behavior of measured channel amplitudes, the amplitude of each channel impulse response bin is fitted into several different distributions using the best fit procedure. It was difficult to visually make conclusion which distribution is the best fit, so our conclusions are based on the maximum log-likelihood test and sum of squares due to errors (SSE) test. Five distributions are used to fit the measured data, including Gaussian, lognormal, Nakagami, Ricean, and Weibull distributions. For the LoS measurement scenario, we have tested statistical properties of the amplitude at distances

ranging from 5 cm to 70 cm. For all tested amplitudes, the closest fit is observed between the measured data and lognormal distribution. To illustrate these results, Figure 14 compares the inverse cumulative distribution function (i.e., quantile plot) of the measured received amplitude of the first bin at the distance  $d = 70$  cm with the inverse cumulative distributions of the Gaussian, lognormal, Ricean, Nakagami, and Weibull distributions. The results in Fig. 14 show that the best fit is between the measured amplitude and the lognormal distribution, which is further verified by having the highest log-likelihood. Similar statistical analysis is performed for NLoS type of propagation where the distance between the  $T_x$  and the  $R_x$  was 30 cm. Similarly, the best fit is observed between the measured data and the lognormal distribution.

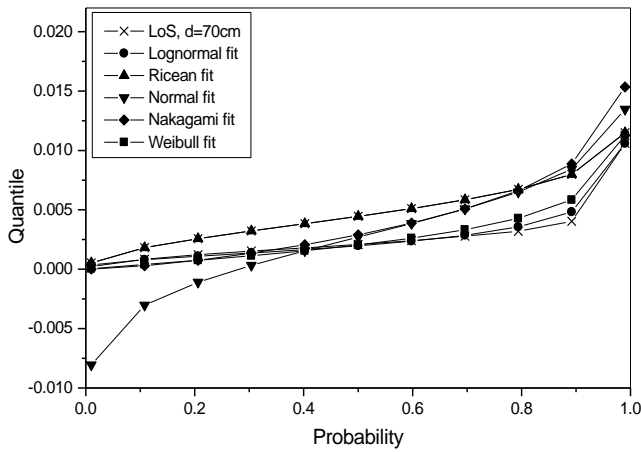


Fig. 14. Theoretical and empirical inverse cumulative distribution functions of channel magnitude in LoS propagation environment.

Finally, we also analyze temporal correlation function in LoS and NLoS propagation environment. The normalized temporal correlation function is calculated as

$$R(\tau) = \frac{E[h(t)h(t+\tau)^*]}{\sqrt{E[|h(t)|^2]E[|h(t)|^2]}}, \quad (8)$$

where  $(\cdot)^*$  denotes complex conjugate operation and  $E[\cdot]$  is the statistical expectation operator.

Figure 15 shows the temporal correlation function in LoS environment for distances  $d = \{5, 10, 40\}$  cm between the  $T_x$  and the  $R_x$ . The results show that correlation function drops below 0.2 after 0.15 ns for all tested distances.

Figure 16 shows the temporal correlation function in NLoS environment where signals are reflected of FR4, plastic and metal. The results show that similar to LoS environment, correlation function drops below 0.2 after 0.15 ns. However, if the strong reflected paths are present in the channel, correlation function can increase above 0.2 and the signals may get correlated again. This corresponds to the findings in power delay profile where strong reflected paths are present in the channel much after the first path has arrived.

#### IV. CONCLUSION

This paper presented measurements and statistical characterization of 300–320 GHz desktop channels. The measurements

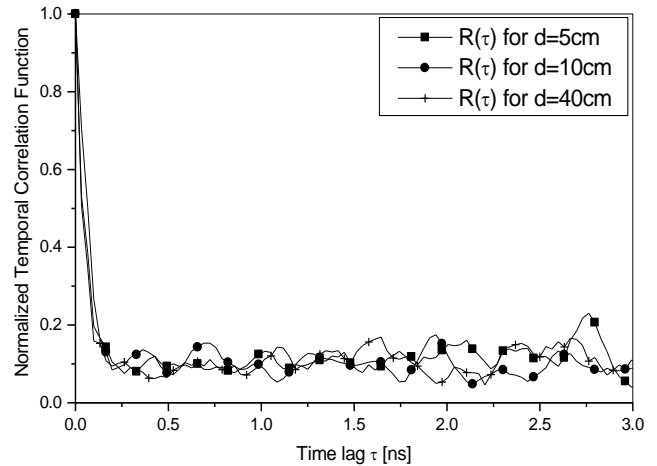


Fig. 15. Normalized temporal correlation function in LOS propagation environment.

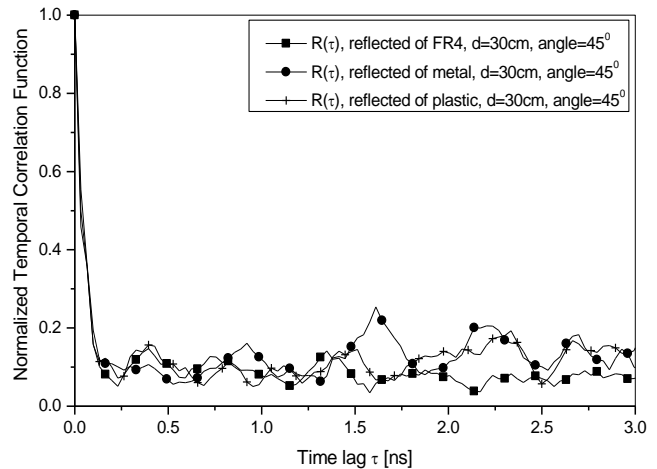


Fig. 16. Normalized temporal correlation function in NLoS propagation environment.

were performed in LoS and NLoS environments. From the large set of LoS measured data, the parameters for single-slope path loss model with shadowing were devised. The results show that the path loss exponent is around 1.9 and the variations due to shadowing are similar across different frequencies and different bandwidths. Furthermore, the impact of different materials on the path loss is studied in NLoS environment. We have found that metal objects in the propagation path cause multiple strong reflections leading to higher path loss. Furthermore, the statistical analysis of multipath propagation is performed. We have calculated the rms delay spread, the mean excess delay, the maximum excess delay, and the coherence bandwidth for LoS and NLoS environments. The results show that the mean excess delay and rms delay spread increase with distance and that the rms delay spread in desktop THz channel is much smaller than in typical indoor ultra-wideband channels. In addition, the power delay profiles for LoS and NLoS environments are analyzed. We have found strong reflections from the transmitter and receiver electronics present both in LoS and NLoS environments. Finally, the statistical analysis of the measured signal amplitude in LoS

and NLoS environments is performed. For both LoS and NLoS propagation environment, it is found that lognormal distribution provides the best fit.

## REFERENCES

- [1] S. Cherry, "Edholms law of bandwidth," *IEEE Spectrum*, vol. 41, pp. 58–60, July 2004.
- [2] P. H. Siegel, "Terahertz technology," *IEEE Transactions on Microwave Theory and Techniques*, MTT-50, pp. 910–928, March 2002.
- [3] T. Kleine-Ostmann, K. Pierz, G. Hein, P. Dawson, and M. Koch, "Audio signal transmission over THz communication channel using semiconductor modulator," *Electronics Letters*, vol. 40, pp. 124–126, January 2004.
- [4] T. Nagatsuma, H. Ito, and T. Ishibashi, "High-power RF photodiodes and their applications," *Laser and Photonics Reviews*, vol. 3, pp. 123–137, March 2009.
- [5] A. Wakatsuki, T. Furuta, Y. Muramoto, T. Yoshimatsu, and H. Ito, "High-power and broadband sub-terahertz wave generation using a J-band photomixer module with rectangular-waveguide output port," *IEEE Proceedings 33th International Conference on Infrared, Millimeter and Terahertz Waves*, pp.1-2, September 2008.
- [6] H. J. Song, K. Ajito, A. Hirata, A. Wakatsuki, Y. Muramoto, T. Furuta, N. Kukutsu, T. Nagatsuma, and Y. Kado, "8 Gbit/s wireless data transmission at 250 GHz," *Electronic Letters*, vol. 45, pp. 1121–U32, October 2009.
- [7] H. -J. Song, K. Ajito, A. Wakatsuki, Y. Muramoto, N. Kukutsu, Y. Kado, and T. Nagatsuma, "Terahertz wireless communication link at 300 GHz," *Proc. Int. Topical Meeting Microw. Photon. (MWP)*, pp. 42–45, 2010.
- [8] J. Ward, E. Schlecht, G. Chattopadhyay, A. Maestrini, J. Gill, F. Maiwald, H. Javadi, and I. Mehdi, "Capability of THz sources based on schottky diode frequency multiplier chains," *IEEE MTT-S Digest*, pp. 1587–1590, 2004.
- [9] T. W. Crowe, W. L. Bishop, D. W. Porterfield, and J. L. Hesler, "Integrated terahertz sources and receivers," *Proceedings IEEE 29th International Conference on Infrared and Millimeter Waves and 12th International Conference on Terahertz Electronics*, pp. 85–86, September 2004.
- [10] C. Jastrow, K. Münter, R. Piesiewicz, T. Kürner, M. Koch, and T. Kleine-Ostmann, "300 GHz transmission system," *Electronic Letters*, vol. 44, pp. 213–U15, January 2008.
- [11] C. Jastrow, S. Priebe, B. Spitschan, J. Hartmann, M. Jacob, T. Kürner, T. Schrader, and T. Kleine-Ostmann, "Wireless digital data transmission at 300 GHz," *Electronic Letters*, vol. 46, pp. 661–U87, April 2010.
- [12] S. Priebe, C. Jastrow, M. Jacob, T. Kleine-Ostmann, T. Schrader, T. Kürner, "Channel and propagation measurements at 300 GHz," *IEEE Transactions on Antennas and Propagation*, vol. 59, no. 5, pp. 1688–1698, May 2011.
- [13] R. Piesiewicz, T. Kleine-Ostmann, N. Krumbholz, D. Mittleman, M. Koch, J. Schoebel, and T. Kürner, "Short-range ultra-broadband terahertz communications: Concepts and perspectives," *IEEE Antennas and Propagation Magazine*, vol. 49, pp. 24–39, June 2007.
- [14] R. Piesiewicz, C. Jansen, D. Mittleman, T. Kleine-Ostmann, M. Koch, and T. Kürner, "Scattering analysis for the modeling of THz communication systems," *IEEE Transactions on Antennas and Propagation*, vol. 55, pp. 3002–3009, November 2007.
- [15] Y. Yang, M. Mandehgar, and D. Grischkowsky, "Broadband THz pulse transmission through the atmosphere," *IEEE Transactions on Terahertz Science and Technology*, vol. 1, pp. 264–273, September 2011.
- [16] J. M. Jornet and I. F. Akyildiz, "Channel modeling and capacity analysis for electromagnetic wireless nanonetworks in the terahertz band," *IEEE Transactions on Wireless Communications*, vol. 10, pp. 3211–3221, October 2011.
- [17] R. Piesiewicz, T. Kleine-Ostmann, N. Krumbholz, D. Mittleman, M. Koch, and T. Kürner, "Terahertz characterisation of building materials," *IEEE Electronic Letters*, vol. 41, pp. 1002–1004, 2005.
- [18] C. Jansen, R. Piesiewicz, D. Mittleman, T. Kürner, and M. Koch, "The impact of reflections from stratified building materials on the wave propagation in future indoor terahertz communication systems," *IEEE Transactions on Antennas and Propagation*, vol. 56, no. 5, pp. 1413–1419, 2008.
- [19] S. Priebe, M. Jacob, C. Jastrow, T. Kleine-Ostmann, T. Schrader, and T. Kürner, "A comparison of indoor channel measurements and ray tracing simulations at 300 GHz," *Proc. Int. Conf. Infrared Millim. Terahertz Waves (IRMMW-THz)*, 2010.
- [20] <http://www.kratosepd.com/> /media/EP/Datasheets/
- [21] <http://www.nordengroup.com/products/frequency-multipliers/frequency-multiplier-33-to-50-ghz/>
- [22] <http://vadiodes.com/index.php/en/products/broadband-multipliers/10-products/165-wr65x3>
- [23] <http://www.vadiodes.com/index.php/en/12-product/126-wr28shm12>
- [24] T. Rappaport, *Wireless communications: principles and practice*, Upper Saddle River, NJ, USA: Prentice Hall PTR, 2001.
- [25] A. G. Zajić, *Mobile-to-Mobile Wireless Channels*. Artech House, Boston MA, January 2013.



**Seunghwan Kim** (S'14) Seunghwan Kim was born in Seoul, South Korea, in 1986. He received Bachelor of Applied Science in Electrical Engineering (with Distinction) from University of Waterloo, Canada, in 2009. During his degree, he has worked as a Research Assistant at the Telecommunication Group of Korea Electrotechnology Research Institute (KERI), and as a Hardware Engineer at Mitel Networks. He is currently pursuing the Ph.D. degree in Electrical Engineering at Georgia Institute of Technology in the area of future ultra-broadband

THz communication systems.



**Alenka G. Zajić** (S'99-M'09-SM'13) Alenka Zajić received the B.Sc. and M.Sc. degrees from the School of Electrical Engineering, University of Belgrade, in 2001 and 2003, respectively. She received her Ph.D. degree in Electrical and Computer Engineering from the Georgia Institute of Technology in 2008. Currently, she is an Assistant Professor in School of Electrical and Computer Engineering at Georgia Institute of Technology. Prior to that, she was visiting faculty in School of Computer Science at Georgia Institute of Technology, a post-doctoral fellow in the Naval Research Laboratory, and design engineer at Skyworks Solutions Inc. Her research interests span areas of electromagnetics, wireless communications, signal processing, and computer engineering.

Dr. Zajić received the Neal Shepherd Memorial Best Propagation Paper Award, the Best Paper Award at ICT 2008, the Best Student Paper Award at WCNC 2007, and was also the recipient of the Dan Noble Fellowship in 2004, awarded by Motorola Inc. and IEEE Vehicular Technology Society for quality impact in the area of vehicular technology. Currently, she is an editor for IEEE Transactions on Wireless Communications.